JOURNAL OF GUIDANCE, CONTROL, AND DYNAMICS
Vol. 32, No. 1, January–February 2009

Autonomous Inertial Relative Navigation with Sight-Line-Stabilized Integrated Sensors for Spacecraft Rendezvous

Hari B. Hablani*
The Boeing Company, Huntington Beach, California 92647

DOI: 10.2514/1.36559

This paper presents a novel autonomous inertial relative navigation technique with a sight-line-stabilized integrated sensor system for midrange (20–1 km) spacecraft rendezvous. A continuous-discrete six-state extended Kalman filter is developed for this purpose. The integrated sensor suite onboard an active chaser satellite comprises an imaging sensor, a coboresighted laser range finder, the space-integrated Global Positioning System/inertial navigation system, and a star tracker. For high accuracy of the relative navigation, the Kalman filter state vector consists of the *inertial* position and velocity of the client satellite governed by a high-fidelity nonlinear orbital dynamics model. The error covariance matrix is formulated in terms of the estimation error in the *relative* position and velocity of the client satellite, consistent with the sensor measurements. Inertial attitude pointing and rate commands for tracking the client satellite are determined using the estimates of the client's inertial relative position and velocity. To estimate the inertial attitude of the chaser satellite outside the space-integrated Global Positioning System/inertial navigation system, a new three-axis steady-state analytical attitude estimator is developed that blends the gyro- and the star-tracker-measured attitudes. The simulation results of a midrange spacecraft rendezvous using glideslope guidance validate this new six-state autonomous inertial relative navigation technique. The simulation results show that the imaging sensor's sight line can be stabilized at the client satellite in midrange accurately enough to enable the laser range finder to measure the range occasionally, but these measurements are not necessary for the midrange rendezvous phase, because the extended Kalman filter can estimate the range with the angle measurements of the imaging sensor.

I. Introduction

THE principal objective of this paper is to present a sight-line-stabilized integrated sensor system that enables novel autonomous inertial relative navigation of a passive client spacecraft for the midrange (20–1 km) phase of a spacecraft rendezvous. Bryan [1] explains various facets of autonomous rendezvous and docking, including its different phases and required sensors. The sensor suite considered here is based on the scenario that the client spacecraft is passive, disabled, or noncooperative, and so there is no cross-link communication between the two satellites nor are there any optical reflective geometry on the client satellite. As such, following [2,3], the selected sensor suite is an integrated sensor system composed of an imaging sensor with wide, medium, and narrow fields of view for relative angle measurements, a coboresighted (or collimated) laser range finder (LRF) for range measurement, and the space-integrated Global Positioning System/inertial navigation system (SIGI) for the active chaser satellite. A new autonomous relative navigation algorithm that this sensor ensemble facilitates is formulated in an inertial frame using a continuous-discrete extended Kalman filter (EKF). To enhance accuracy of attitude estimates of the chaser satellite, the SIGI Kalman filter is provided with star tracker measurements of the inertial attitude of the satellite. For attitude estimation outside the SIGI, a new three-axis steady-state attitude estimator is developed that optimally blends gyro and star tracker attitude measurements. The inertial relative position and velocity estimates of the client satellite are used to determine the pointing and rate commands for tracking. A three-axis attitude controller stabilizes the imaging sensor's sight line and coboresighted LRF at the client satellite within the pointing-accuracy requirements. Whereas the field of view of an imaging sensor is large (4×4 deg for medium and 1×1 deg for narrow fields of view), the laser beam width is merely $\sim$0.25 mrad (0.014 deg) and has very low divergence ($\sim$0.25 mrad) [3]. Therefore, whereas the pointing requirement to avoid jitter of the imaging sensor is loose, that for the LRF is stringent (15–30 μrad). For accurate pointing, the imaging-sensor boresight and the coboresighted LRF must be aligned very carefully [2,3]. Because achieving this degree of alignment and pointing stability is expensive, a secondary objective of this study is to show that it is not necessary to measure the range for a midrange (20–1 km) rendezvous, because it can be estimated from the angle measurements under certain observability conditions [4,5].

The present proof-of-concept study differs from the studies and flight tests of the past in several respects. Kawano et al. [6] illustrated the use of relative Global Positioning System (GPS) and laser radar navigation for the relative approach phase (from 10 km to 500 m) and final approach phase (from 550 to 2 m) of autonomous rendezvous and docking of two engineering test satellites (ETS-VII). The satellites were equipped with GPS receivers and cross-link antennas. Similarly, Park et al. [7] developed a relative navigation Kalman filter for rendezvous of the space shuttle with the wake-shield facility, both vehicles having GPS receivers and the wake-shield facility transmitting its receiver's output to the orbiter; the electro-optic sensors were not involved in this test. In their more recent demonstration of the Rendezvous and Proximity Operation Program, Clark et al. [8] illustrated the benefits of their relative navigation Kalman filter using an LRF when the two spacecraft were within the range of a few hundred meters. Here again, because of the short range, the pointing accuracy of the sensors was not a concern, and relative navigation was based on simple linear relative dynamics in the local-vertical/local-horizontal (LVLH) frame. Gaylor and Lightsey [9] emulated the SIGI Kalman filter for operation in proximity of the International Space Station, but they did not deal with relative navigation or electro-optic sensors and their pointing. Woffinden and Geller [10] formulated relative navigation using angles only, but their study was for very close range (25 m) in which

Presented as Paper 5355 at the AIAA Guidance, Navigation, and Control Conference and Exhibit, Austin, TX, 11–14 August 2003; received 9 January 2008; revision received 28 May 2008; accepted for publication 29 May 2008. Copyright © 2008 by The Boeing Company. All rights reserved.. Published by the American Institute of Aeronautics and Astronautics, Inc., with permission. Copies of this paper may be made for personal or internal use, on condition that the copier pay the $10.00 per-copy fee to the Copyright Clearance Center, Inc., 222 Rosewood Drive, Danvers, MA 01923; include the code 0731-5090/09 $10.00 in correspondence with the CCC.

*Technical Fellow, Integrated Defense Systems, Flight Sciences and Advanced Design; currently Visiting Faculty, Department of Aerospace Engineering, Indian Institute of Technology, Kanpur 208 016, India. Associate Fellow AIAA.

the target image nearly filled the sensor's focal plane and estimation of the target's relative attitude was important for docking. To sum up, there does not appear to be a study or flight test in the past that involved the sensor ensemble considered in the present study, with the target as a point source, relative navigation in the inertial frame, Kalman filter for estimating inertial attitude of the bus using gyros and star tracker, SIGI for inertial navigation, and glideslope guidance of the spacecraft from a range of 20 to 1 km relative to the client spacecraft.

The layout of this paper is as follows. Section II presents the overall architecture of autonomous inertial relative navigation for midrange rendezvous using the integrated sensor system, a continuous-discrete extended Kalman filter, pointing and rate commands for tracking, a steady-state three-axis attitude estimator, and a three-axis attitude controller. Section III presents the inertial relative navigation formulation. The relative navigation is in the inertial frame, not the LVLH frame, for the reasons explained therein. The continuous-discrete EKF is developed for the inertial relative navigation, and nonlinear orbital dynamics are employed to propagate the inertial position and velocity estimates of the client satellite. Using relative position and velocity estimates of the client satellite, Sec. IV develops pointing and rate commands to track the client with the integrated sensor package. Section V presents an analytical three-axis steady-state attitude estimator to blend gyro measurements with the star tracker measurements and produce the optimal inertial attitude of the bus carrying the sensor package. Section VI illustrates an application of the preceding inertial relative navigation system to a rendezvous mission in which the chaser satellite translates under glideslope guidance from an initial relative position of -18, -8, and 10 km to a final position of -1, 0, and 1 km in the client satellite's LVLH frame. Section VII concludes the paper.

II. Overall Architecture of Autonomous Inertial Relative Navigation with Integrated Sensors

Figure 1 portrays the overall closed-loop architecture of the autonomous inertial relative navigation of the client satellite with the integrated sensor system composed of the SIGI, a star tracker, an imaging sensor, and a coboresighted laser range finder. The SIGI [11–13] provides the inertial position, velocity, attitude, and rate of the chaser satellite bus at 50 Hz frequency. The imaging sensor provides the azimuth and elevation of the point-mass client satellite relative to the sensor's focal-plane axes at 1 Hz frequency. If the imaging sensor is pointed accurately enough (specified next), then the laser range finder provides the range measurement of the client satellite. The client satellite is a passive, disabled, noncooperative satellite, with no GPS receiver or intersatellite communication ability, and so the differential GPS cannot be used for relative navigation. Instead, a continuous-discrete EKF is developed for this purpose, which uses line-of-sight angles and, possibly, the range measurements. The *continuous* part of the navigation filter is implemented as 50 Hz propagation of the state estimate consisting of the client satellite's position and velocity. Accuracy of the attitude estimates from the SIGI is enhanced by using the star tracker measurements [12] at 6 s intervals ($\frac{1}{6}$ Hz frequency). In Fig. 1 and later in the simulation, the SIGI star tracker attitude estimation process is emulated with a new three-axis steady-state attitude Kalman filter developed in Sec. V, and it provides the attitude and rate estimates for attitude control at 25 Hz.

Briefly, the closed-loop guidance, inertial relative navigation, pointing and tracking system portrayed in Fig. 1 for rendezvous operates as follows. The target is first acquired with an imaging sensor using some acquisition methodology [3]. Whereas the required pointing accuracy for the imaging sensor is not stringent, that for the collimated LRF is 75 μrad per axis (1σ) at a 10 km distance. Any misalignment between the focal-plane boresight and the LRF beam is precalibrated with precision ($\sim$20 μrad). Because pointing accuracy of the imaging sensor is insensitive to its small misalignments with the gyros and star tracker [14], that misalignment is precalibrated with lesser precision. The 1 Hz azimuth and elevation measurements are used along with the inertial attitude estimates of the bus in the inertial relative navigation Kalman filter to estimate the inertial position and velocity of the client satellite. Subtracting the inertial position and velocity estimates of the chaser satellite from those of the client satellite, the relative position and velocity estimates of the client satellite are obtained, which are then used to calculate the pointing commands and rates to track the client satellite. The attitude of the chaser spacecraft is controlled and the sight line of

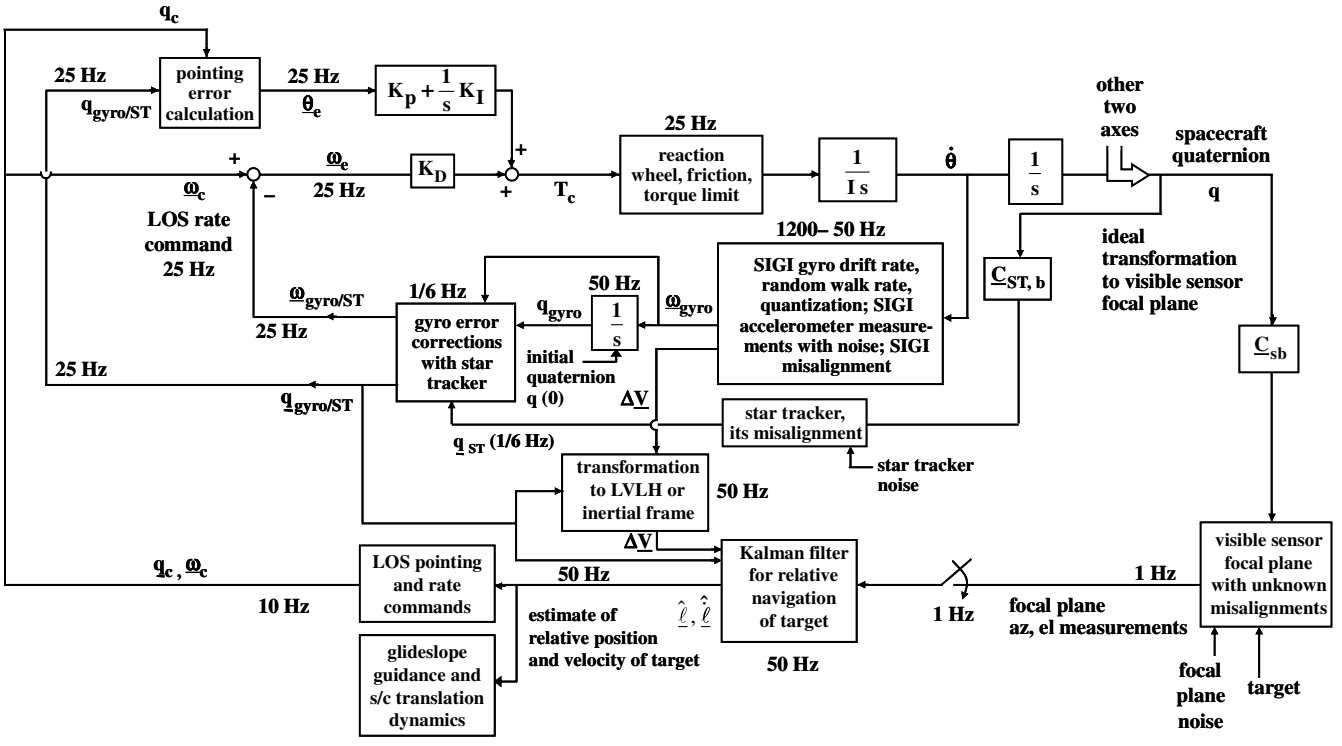

Fig. 1 SIGI imaging sensor and laser-range-finder pointing architecture for relative navigation and guidance for rendezvous (az denotes azimuth, el denotes elevation, and s/c denotes the spacecraft.

the imaging sensor is stabilized with a proportional–integral–derivative (PID) controller and reaction wheels operating at 25 Hz [14,15]. The calculation of pointing error $\underline{\theta}_e$ and its interesting relationship with the focal-plane azimuth- and elevation-angle measurements (actually, their estimates) is revealed in Sec. IV. The glideslope guidance law [16] determines the periodic $\Delta\underline{V}$ firings every 60 s to bring the chaser spacecraft closer to the client spacecraft with an exponential decrease in its relative position and relative velocity. The $\Delta\underline{V}$ are measured by the three orthogonal accelerometers of the inertial navigation system (INS), and the SIGI determines the inertial position and velocity of the chaser satellite at 50 Hz. These are used in the continuous-discrete EKF to determine the inertial relative position and velocity of the client satellite, as just explained, at 50 Hz. Each of the preceding aspects of inertial relative navigation is formulated and elaborated in the subsequent sections.

Although the LRF is coboresighted with the imaging sensor for range measurement, [5] shows that as long as there is some relative altitude between the two spacecraft, the in-track component of the range is observable via the in-plane angle measurements. See [4,17,18] for observability of the inertial position and velocity of the spacecraft via inertial line-of-sight angle measurements. This will be illustrated with simulation results in Sec. VI. Hence, a laser range finder is not essential for range measurement until the distance between the two satellites becomes too short (less than 1 km) to be safe without it. At such close distances, though, the client satellite's image fills the focal plane of the sensor, and the pointing requirements for both the imaging sensor and the LRF become relatively loose and the attitude control becomes relative easy.

III. Six-State Relative Navigation of the Client Satellite in the Inertial Frame

Our objective now is to develop a six-state continuous-discrete extended Kalman filter to estimate the inertial position and velocity of the client satellite relative to the chaser satellite. The formulation is in the inertial frame, not the LVLH, for three reasons. First, a large relative in-track distance of 20 km between the two spacecraft at an altitude of 500 km is equal to an orbital arc of ~3 mrad, which is much larger than the imaging-sensor noise 0.07 mrad (1σ) for a point target, and therefore a 3 mrad arc cannot be treated as a nominal horizontal boresight of the imaging-sensor focal plane, and even more so for the pencil laser beam. Second, at a 10 km relative range, [19] shows that the linearization of even the spherical differential gravity between the two vehicles causes significant navigation errors. To illustrate the errors for low-altitude 100 min orbits, consider a two-pulse rendezvous scenario in Fig. 2, in which a chaser satellite is ~18 km behind and 10 km below a client satellite at a 500 km altitude, and starting with a guidance pulse at $t = 0$, it reaches 1 km behind the client satellite at the same altitude in 1800 s. In the Earth's spherical gravitation field ($J_2 = 0$), the linearization of the differential gravity $\delta\underline{g}\,(r_0, r_1)$ [see Eqs. (13) and (14)] introduces a $\widetilde{\delta\underline{g}}$ estimation error, the three components of which are shown in Fig. 3. We observe that $\|\widetilde{\delta\underline{g}}\|$ is ~0.1 mm/s^2 at $t = 0$ and it approaches zero as the chaser approaches the client satellite. But even this minute $\widetilde{\delta\underline{g}}$ error develops a relative position estimation error greater than 100 m in 1800 s, as shown in Fig. 4 in the client satellite's LVLH frame. This error is open-loop in that it is in the absence of measurements and a recursive estimation process; nevertheless, it suggests the inadequacy of the linearized relative dynamics model. Consequently, our use of this linearization for long distances in [16], in retrospect, is an error.

The third reason is concerned with the Earth's nonspherical gravity. The error in Fig. 4 would be aggravated if the orbital dynamics model ignores the most predominant J_2 gravitational acceleration, which causes regression of the orbital ascending node and perturbs the satellite's nominal position at twice the orbital frequency. For example, for a 500 km altitude orbit with 46 deg inclination, the average ascending-node regression rate is 1 μrad/s. In 1800 s (a typical duration to decrease the in-track distance from 20 to 1 km), the ascending node regresses by ~12 km on the average.

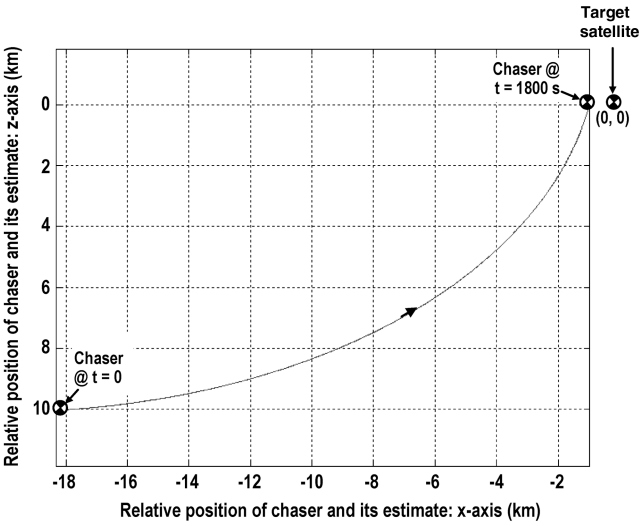

Fig. 2 Trajectory of a chaser satellite with one initial pulse and its estimate relative to the client satellite LVLH frame.

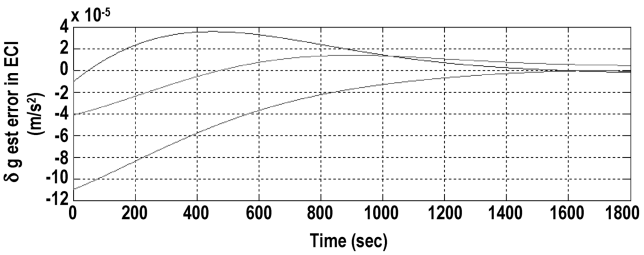

Fig. 3 Differential gravitational acceleration estimation error due to linearization.

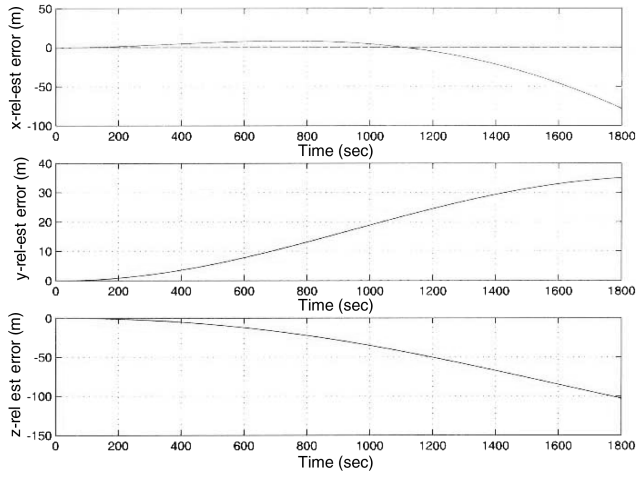

Fig. 4 Relative position estimation error due to linearization of the spherical gravity field.

The attendant exact perturbations in the spacecraft position from the ideal circular orbit would depend on its initial location in the orbit, but the 12 km average nodal regression while the relative in-track distance decreases from 20 to 1 km is clearly too significant to ignore and to use the LVLH frame for relative navigation. (We have not determined the relative position estimation error with J_2, similar to the error in Fig. 4, however.)

For these reasons, we use a geocentric inertial frame and a gravity model that includes the J_2 term to propagate the orbits of both vehicles. The higher-order gravitational accelerations are ignored in this study.

Some features of the continuous-discrete EKF for inertial relative navigation of the client satellite presented here are different from its

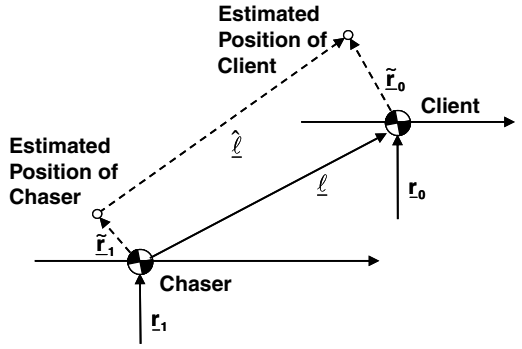

Fig. 5 True and estimated inertial positions of the chaser and the target, true and estimated relative positions of the target, and inertial position estimation errors of the chaser and the target.

textbook counterpart [20]. The azimuth and elevation angles are related to the relative position of the client satellite. In the EKF presented here, this relative position is obtained by differencing the inertial positions of the two satellites, as stated earlier. Whereas the chaser satellite's inertial position estimate is provided by the SIGI, the inertial position of the client satellite is estimated by the filter. Thus, the system dynamics model in the filter consists of the orbital dynamics of the client satellite, and the state vector is 6×1. In contrast, the state vector of the standard EKF would involve orbital dynamics of both satellites, and the state vector would be 12×1 as in [4]. Further, because the measurements are related to the relative position of the client satellite, the linearized measurement matrix $\underline{H}$, the transition matrix $\underline{\Phi}$, and the error covariance matrix $\underline{P}$ are all related to the relative position vector, not to the inertial position. The salient features of the present continuous-discrete EKF are summarized next.

A. Six-State Inertial Relative Navigation Formulation

Figure 5 shows a client satellite and a chaser satellite in two neighboring circular orbits. The radial vectors $\underline{r}_1$ and $\underline{r}_0$ from the Earth's mass center denote inertial positions of the chaser and the client satellite, respectively, governed by the following equations in the geocentric inertial frame:

$$\ddot{\underline{r}}_1 = \underline{g}(\underline{r}_1) + \underline{a}_1 \tag{1}$$

$$\ddot{\underline{r}}_0 = \underline{g}(\underline{r}_0) \tag{2}$$

where $\underline{g}$ is the total (spherical plus nonspherical) Earth's gravitational acceleration, and $\underline{a}_1$ is the acceleration of the chaser satellite caused by the thrusters for guidance. The estimate $\hat{r}_0$ of the client's position in the inertial frame is governed by a similar equation:

$$\ddot{\hat{r}}_0 = \underline{g}(\hat{r}_0) \tag{3}$$

This equation, rewritten in its first-order form with the state vector as $[\hat{r}_0;\ \dot{\hat{r}}_0]$, is used in the continuous-discrete EKF for the client satellite's state estimate propagation at 50 Hz. On the other hand, the estimates of the chaser satellite's inertial position and velocity, $\hat{r}_1$ and $\dot{\hat{r}}_1$, are furnished by its SIGI, as stated earlier. An estimate of the position and velocity of the client satellite relative to the chaser satellite is then

$$\hat{\ell} = \hat{r}_0 - \hat{r}_1 \tag{4}$$

$$\dot{\hat{\ell}} = \dot{\hat{r}}_0 - \dot{\hat{r}}_1 \tag{5}$$

where $\underline{\ell}$ stands for the line-of-sight vector of the imaging sensor mounted on the chaser satellite bus. The associated estimation errors in terms of the estimation errors in $\hat{r}_1$, $\hat{r}_0$, $\dot{\hat{r}}_1$, and $\dot{\hat{r}}_0$ are

$$\tilde{\ell} = \tilde{r}_0 - \tilde{r}_1 \tag{6}$$

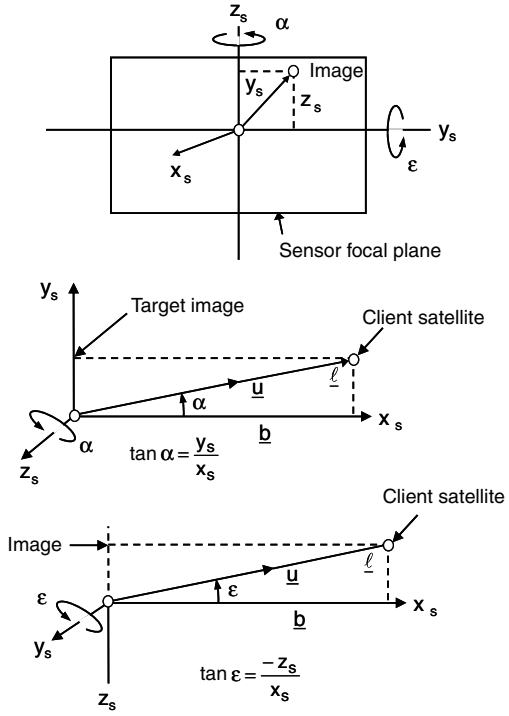

Fig. 6 Two-axis pointing angle commands to align the focal-plane boresight with the line of sight to the client satellite.

$$\dot{\tilde{\ell}} = \dot{\tilde{r}}_0 - \dot{\tilde{r}}_1 \tag{7}$$

where the chaser navigation estimation errors $\tilde{r}_1$ and $\dot{\tilde{r}}_1$ are the SIGI navigation errors.

Because the imaging sensor of the chaser satellite measures azimuth and elevation angles of the client satellite at 1 Hz frequency (the angles illustrated in Fig. 6 and explained in Sec. IV), and because these measurements depend on the relative position vector $\underline{\ell}$, not $\underline{r}_1$ and $\underline{r}_0$ individually, it is convenient to perform the measurement updates of the relative vectors $\hat{\ell}$ and $\dot{\hat{\ell}}$. The Kalman gain $\underline{K}$ is required for this update, and its evaluation, in turn, requires the measurement sensitivity matrix $\underline{H}$ and the error covariance matrix $\underline{P}$. $\underline{H}$ will be formulated subsequently [Eq. (23)]. The 6×6 error covariance matrix $\underline{P}$ for the relative position and velocity estimation errors $\tilde{\ell}$ and $\dot{\tilde{\ell}}$ is defined as

$$\underline{P} = E\left(\begin{bmatrix}\tilde{\ell}\\ \dot{\tilde{\ell}}\end{bmatrix}[\tilde{\ell} \quad \dot{\tilde{\ell}}]\right) \tag{8}$$

and propagated at 50 Hz as follows:

$$\underline{P}_i(-) = \underline{\Phi}\underline{P}_{i-1}(+)\underline{\Phi}^T + \underline{Q} \tag{9}$$

where $E(\cdot)$ is the expectation operator, $\underline{\Phi}$ is the 6×6 transition matrix, and $\underline{Q}$ is the 6×6 process noise matrix. The discrete propagation of $\underline{P}$ at 50 Hz is our replacement of the continuous propagation of $\underline{P}$ in the standard continuous-discrete EKF algorithm.

Markley [21] developed an easily computable 6×6 Cartesian state transition matrix $\underline{\Phi}$ as a function of the gradient matrix $\underline{G}$ of the gravitational acceleration, evaluated both at the beginning and at the end of the propagation interval (20 ms, presently). Because the sensor measurements are used to update $\hat{\ell}$ (and $\dot{\hat{\ell}}$) and the line-of-sight vector $\underline{\ell}$ originates from the chaser sensor at the inertial position $\underline{r}_1$, the transition matrix $\underline{\Phi}$ is evaluated at the estimates $\hat{r}_1(t_{i-1})$ and $\hat{r}_1(t_i)$ provided by the SIGI. Clearly, the navigation errors of the SIGI influence the $\underline{\Phi}$ and hence $\underline{P}$. The process noise matrix $\underline{Q}$, formulated subsequently, accounts for these and other modeling errors. The 6×6 transition matrix $\underline{\Phi}$ is given by [21]

$$\underline{\Phi} = \underline{\Phi}(\hat{r}_1(t_i), \hat{r}_1(t_{i-1})) = \begin{bmatrix} \underline{\Phi}_{rr} & \underline{\Phi}_{rv} \\ \underline{\Phi}_{vr} & \underline{\Phi}_{vv} \end{bmatrix} \tag{10}$$

where t_{i-1} and t_i are, respectively, the beginning and the end of the current 50 Hz sample period, and

$$\underline{\Phi}_{rr} = \underline{I} + (2\underline{G}_{i-1} + \underline{G}_i)(\Delta t)^2/6 \tag{11a}$$

$$\underline{\Phi}_{rv} = \underline{I}\Delta t + (\underline{G}_{i-1} + \underline{G}_i)(\Delta t)^3/12 \tag{11b}$$

$$\underline{\Phi}_{vr} = (\underline{G}_{i-1} + \underline{G}_i)\Delta t/2 \tag{11c}$$

$$\underline{\Phi}_{vv} = \underline{I} + (\underline{G}_{i-1} + 2\underline{G}_i)(\Delta t)^2/6 \tag{11d}$$

where $\underline{I}$ is a 3×3 identity matrix, and $\underline{G}_{i-1}$ and $\underline{G}_i$ are the gravity gradient matrices evaluated at t_{i-1} and t_i respectively. Markley [21] furnishes the 3×3 gradient matrix $\underline{G}$ up to the J_2 gravitational term, and to conserve space, it will not be reproduced here. Montenbruck and Gill [22] provide the gradient matrix of a much higher order for high-fidelity simulations, though that will not be used in this study.

Digressing for a moment, note that if the change in the gradient matrix from $\hat{r}_1(t_{i-1})$ to $\hat{r}_1(t_i)$ is ignored (that is, suppose $G_{i-1} = G_i$) and, further, if the second- and higher-order terms in Δt are ignored as well in submatrices (11), then the transition matrix $\underline{\Phi}$ simplifies to

$$\underline{\Phi} = \begin{bmatrix} \underline{I} & \underline{I}\Delta t \\ \underline{G}_i\Delta t & \underline{I} \end{bmatrix} = \underline{I}_{6\times6} + \begin{bmatrix} \underline{0} & \underline{I} \\ \underline{G}_i & \underline{0} \end{bmatrix}\Delta t = I_{6\times6} + \underline{A}\Delta t \tag{12}$$

where $I_{6\times6}$ is a 6×6 identity matrix, and the definition of the 6×6 matrix $\underline{A}$ is apparent. The $\underline{A}$ is indeed the state-space matrix that governs the linearized dynamics of the 6×1 relative state vector $[\hat{\ell};\ \dot{\hat{\ell}}]$. The second-order version of this approximate linear state-space equation of the relative motion is

$$\ddot{\hat{\ell}} \approx \underline{G}(\hat{r}_1)\hat{\ell} - \hat{a}_1 \tag{13}$$

where $\hat{a}_1$ is the estimate of the thruster acceleration $\underline{a}_1$. The exact nonlinear counterpart of Eq. (13) is obtained from the estimation version of Eqs. (1) and (2):

$$\ddot{\hat{\ell}} = \underline{g}(\hat{r}_0) - \underline{g}(\hat{r}_1) - \hat{a}_1 \tag{14a}$$

$$= \delta\underline{g}(\hat{r}_0, \hat{r}_1) - \hat{a}_1 \tag{14b}$$

where $\delta\underline{g}(\hat{r}_0, \hat{r}_1)$ is the estimated differential gravity. When linearized, $\delta\underline{g}(\hat{r}_0, \hat{r}_1) \approx G(\hat{r}_1)\hat{\ell}$, as seen in Eq. (13). The estimation error $\widetilde{\delta g}$, illustrated earlier in Fig. 3, is the difference between the exact $\delta\underline{g}(\underline{r}_0, \underline{r}_1)$ and its linear approximation $G(\underline{r}_1)\underline{\ell}$ for the spherical gravitational field (J_2 and higher-order terms being zero). Equation (14a) also reveals why this equation is not used directly in the EKF and Eq. (3) is used instead: solving Eq. (14a) requires a priori knowledge of the inertial positions $\hat{r}_0$ and $\hat{r}_1$, which comes from the integration of Eq. (3) and the SIGI, respectively, but that renders Eq. (14a) superfluous.

Returning to the state estimate updates at the time of sensor measurements, the updates of the Kalman gain matrix and the error covariance matrix $\underline{P}$ take place at 1 Hz, and the relative position and velocity vector estimates are updated from $\hat{\ell}(-)$ to $\hat{\ell}(+)$ and $\dot{\hat{\ell}}(-)$ to $\dot{\hat{\ell}}(+)$, respectively. Knowing the concurrent inertial position and velocity estimates of the chaser satellite provided by the SIGI, the inertial position and velocity estimates of the client satellite are updated as follows:

$$\hat{r}_0(+) = \hat{\ell}(+) + \hat{r}_1 \tag{15a}$$

$$\dot{\hat{r}}_0(+) = \dot{\hat{\ell}}(+) + \dot{\hat{r}}_1 \tag{15b}$$

The recursive nonlinear propagation of these estimates then continues with the integration of Eq. (3). It is also clear from the preceding formulation that the SIGI navigation errors infiltrate the client satellite's position and velocity estimation process.

B. SIGI Navigation Errors of the Chaser Satellite: A Simple Model

A detailed accurate model of the SIGI navigation errors is not available in public domain. Zubkow [12], for example, simply states that the blended GPS/INS performance of the SIGI system in the precise positioning service mode is 16 m spherical error probability in position and 0.1 m/s in velocity and does not offer any model. More details on the GPS errors can be gleaned from [22,23]. These errors are partly due to the gyros and accelerometers and partly due to the GPS system, both filtered by the SIGI's internal tightly coupled high-fidelity navigation Kalman filter. Misra and Enge [23] describe the GPS navigation errors as consisting of biases and zero-mean noises. The biases are due to the satellite clock errors, ephemeris errors (3 m rms), and atmospheric propagation modeling errors (5 m rms), changing slowly as the GPS satellites' elevation angles change; the zero-mean noises, on the other hand, are due to the receiver noise and multipath of GPS signals (1 m rms). The combined user range error is ~6 m rms [23]. In this work, our intent is not to develop a high-fidelity model of the preceding error sources. Instead, we will represent the SIGI navigation errors simply with an aggregate model as follows.

The position errors along the local-horizontal x and y axes are each modeled as a first-order exponentially correlated Markov process, following [24]. For example, the error along the x axis is

$$x_e = H_{\text{dop}}(b_x + \nu_x) \tag{16}$$

where b_x is a bias error, ν_x is a random error, and the horizontal dilution of precision $H_{\text{dop}} = 1.2$ [17,25]; b_x and ν_x are each first-order exponentially correlated Markov processes. For example, the discrete version of the bias $b_{x,i}$ is governed by

$$b_{x,i} = b_{x,i-1}\exp(-\beta_b\Delta t) + w_{b,i-1} \tag{17}$$

where $1/\beta_b$ is the time constant of the process, Δt is the sample period (20 ms, presently), and $w_{b,i}$ is the discrete white noise process with variance equal to $q_b\Delta t$; q_b is the power spectral density of the continuous white noise of which $w_{b,i}$ is the discrete version, and $q_b = 2\sigma_b^2\beta_b$, with σ_b^2 being the variance of the bias b_x. Presently, these parameters are taken as $\sigma_b = 5.1$ m, and $1/\beta_b$ is one-eighth of the orbit period. The exponentially correlated random error ν_x is modeled similarly, with the variance of the discrete white noise that generates it equal to $q_v\Delta t$, $q_v = 2\sigma_v^2\beta_v$, $\sigma_v^2 = (1.4\text{ m})^2$, and $1/\beta_v = 60$ s. The vertical position error z_e is modeled likewise:

$$z_e = V_{\text{dop}}(b_z + \nu_z) \tag{18}$$

where b_z and ν_z are defined as b_x and ν_x are, respectively, with the same numerical parameters; the vertical dilution of precision $V_{\text{dop}} = 1.4$.

The velocity of the satellite is measured by the Doppler shift of the GPS signal frequency. Misra and Enge [23] show that the velocity error could be modeled as a discrete white noise sequence in each axis, with its standard deviation σ_v equal to 0.03 m/s in each axis.

Because the SIGI navigation errors contribute directly to the errors in propagation of the relative position and velocity, the preceding model of the SIGI navigation errors is used to develop a corresponding process noise matrix $\underline{Q}$. The 3×3 process noise matrix $\underline{Q}_{\text{pos}}$ corresponding to the position error in the local-vertical/local-horizontal frame is

$$\underline{Q}_{\text{pos}} = q_{\text{scalar}} \times \text{diag}(q_b + q_n)\Delta t[H_{\text{dop}}^2; H_{\text{dop}}^2; V_{\text{dop}}^2] \tag{19}$$

where q_{scalar} is introduced to tune the filter. The 3×3 velocity process noise matrix $\underline{Q}_{\text{vel}} = q_{\text{scalar}} \times \sigma_v^2\underline{I}$ ($\underline{I} = 3 \times 3$ identity matrix).

C. Focal Plane Angles and Range Measurements

Figures 5 and 6 illustrate relative geometry of the two satellites, the focal plane of the imaging sensor, and the image of the client satellite on the focal plane. Because of imperfect tracking, the client image is at some nonzero azimuth and elevation angles relative to the focal-plane center. Let the line-of-sight (LOS) vector $\underline{\ell}$, expressed in the sensor frame $\mathfrak{F}_s$, have the components $\underline{\ell}^{\mathfrak{F}_S} = [x_S;\ y_S;\ z_S]$. The LOS angle measurements at 1 Hz are thus related to the components of $\underline{\ell}$: Azimuth:

$$\alpha_m = \alpha + \nu_\alpha = \tan^{-1}(y_s, x_s) + \nu_\alpha \tag{20a}$$

Elevation:

$$\varepsilon_m = \varepsilon + \nu_\varepsilon = \tan^{-1}(-z_s, x_s) + \nu_\varepsilon \tag{20b}$$

These angles are much less than 1 rad for the target image to be within the sensor track box. The quantities ν_α and ν_ε are the zero-mean random white noises corrupting the measurements, and their standard deviations would increase as the distance between the two satellites decreases. Using these measurements and the pointing control system shown in Fig. 1, the integrated sensors may be sufficiently accurately pointed at the client satellite so that the collimated laser beam would impinge upon the client and determine its relative range. The required pointing accuracy is about 10–100 μrad (1σ) [3,26], depending on the relative range. The noisy range measurement is modeled as

$$r_m = \|\underline{\ell}\| + \nu_r \tag{21}$$

where ν_r is a zero-mean white noise. For updates of the line-of-sight vector estimates and its rate from $\hat{\ell}(-)$ and $\hat{\dot{\ell}}(-)$ to $\hat{\ell}(+)$ and $\hat{\dot{\ell}}(+)$ with the preceding measurements, the usual 3×1 partial derivative vectors $\partial\alpha/\partial\underline{\ell}$, $\partial\varepsilon/\partial\underline{\ell}$, and $\partial\ell/\partial\underline{\ell}$ are thus derived in the sensor frame and transformed to the inertial frame [24,27]:

$$\frac{\partial\alpha}{\partial\underline{\ell}^{\mathfrak{F}_I}} = \underline{C}_{Is}\frac{\partial\alpha}{\partial\underline{\ell}} \tag{22a}$$

$$\frac{\partial\varepsilon}{\partial\underline{\ell}^{\mathfrak{F}_I}} = \underline{C}_{Is}\frac{\partial\varepsilon}{\partial\underline{\ell}} \tag{22b}$$

$$\frac{\partial\ell}{\partial\underline{\ell}^{\mathfrak{F}_I}} = \underline{C}_{Is}\frac{\partial\ell}{\partial\underline{\ell}} \tag{22c}$$

where $\underline{C}_{Is} = \underline{C}_{Ib}\underline{C}_{bs}$ is the transformation matrix from the sensor frame $\mathfrak{F}_s$ to the inertial frame $\mathfrak{F}_I$, $\underline{C}_{Ib}$ is the transpose of the inertial attitude $\underline{C}_{bI}$ of the spacecraft provided by the SIGI, and $\underline{C}_{bs}$ is the transformation matrix from the ideal sensor frame $\mathfrak{F}_s$ to the chaser bus frame $\mathfrak{F}_b$. Clearly, the gyro and star tracker errors filtered through the SIGI Kalman filter will influence the inertial relative navigation Kalman filter performance. The linearized (3×6) measurement matrix $\underline{H}$ associated with the measurement vector $\underline{z} = [\alpha_m\ \varepsilon_m\ r_m]^T$ for updates of the Kalman gain matrix and the error covariance matrix is

$$\underline{H} = \begin{bmatrix} \left(\frac{\partial\alpha}{\partial\underline{\ell}^{\mathfrak{F}_I}}\right)^T & \\ \left(\frac{\partial\varepsilon}{\partial\underline{\ell}^{\mathfrak{F}_I}}\right)^T & \underline{0}_{3\times3} \\ \left(\frac{\partial\ell}{\partial\underline{\ell}^{\mathfrak{F}_I}}\right)^T & \end{bmatrix} \tag{23}$$

where $\underline{0}_{3\times3}$ is a 3×3 null matrix. Because the slopes on the right side of Eq. (23) are computed with the estimated $\hat{\ell}$ and the inertial attitude estimate $\underline{C}_{Ib}$ of the chaser satellite, the SIGI navigation errors influence the $\underline{H}$ matrix and thereby the estimation accuracy of the navigation Kalman filter.

IV. Pointing Commands

A. Quaternion Commands

Figure 7 shows a client satellite and a chaser satellite in two neighboring circular orbits. The local-vertical/local-horizontal frame at the client satellite mass center is denoted as $\mathfrak{F}_0$, and the one at the chaser satellite mass center is denoted as $\mathfrak{F}_1$. The pointing commands are the attitude commands for the chaser satellite to orient its imaging-sensor boresight to the client satellite. The sensor may be somewhat misaligned from its ideal orientation relative to the chaser satellite's optic bench. These misalignment angles are small (perhaps less than a milliradian) and unknown and not of any particular concern in this paper. Nevertheless, let $\mathfrak{F}_s$ and $\mathfrak{F}'_s$ be the ideal and the misaligned frames of the sensor, respectively, and let $\underline{C}_{ss'}$ transform a vector in the $\mathfrak{F}'_s$ to the frame $\mathfrak{F}_s$. In the misaligned frame $\mathfrak{F}'_s$: $x'_s y'_s z'_s$, the boresight of the sensor is along the x'_S axis and the objective is to point the boresight at the client satellite. Let $\underline{b}$ be a unit vector along the boresight axis. Then, in the frame $\mathfrak{F}'_s$, $\underline{b}^{\mathfrak{F}'_s} = [1;\ 0;\ 0]$. This unit vector is transformed to the chaser body frame $\mathfrak{F}_b$ via the transformation matrix $\underline{C}_{ss'}$ and the transformation matrix $\underline{C}_{bs}$; thus, $\underline{b}^{\mathfrak{F}_b} = \underline{C}_{bs}\, C_{ss'}\, b^{\mathfrak{F}'_s}$. On the other hand, the relative vector $\underline{r}_{10}$ from the chaser center of mass to the client center of mass, expressed in an inertial frame $\mathfrak{F}_I$, is given by $\underline{r}_{10}^{\mathfrak{F}_I} = -\underline{r}_1^{\mathfrak{F}_I} + \underline{r}_0^{\mathfrak{F}_I}$, where $\underline{r}_1$ and $\underline{r}_0$ are both expressed in the frame $\mathfrak{F}_I$. The imaging sensor is located at an offset vector $\underline{r}_{\text{off}}$ from the chaser center of mass (Fig. 7). Hence, the line-of-sight vector from the focal-plane center of the chaser to the client satellite is given by $\underline{\ell} = \underline{r}_{10} - \underline{C}_{Ib}\underline{r}_{\text{off}}$. A unit vector $\underline{u}$ along this line-of-sight vector is given by $\underline{u}^{\mathfrak{F}_I} = \underline{\ell}/\|\underline{\ell}\|$. The offset vector $\underline{r}_{\text{off}}$ is not accounted for in Sec. III, in which $\underline{\ell} = \underline{r}_{10}$. This is acceptable at long ranges, but as the range decreases, neglecting $\underline{r}_{\text{off}}$ introduces a bias error in the command angles and therefore it is considered now. Knowing the estimate $\hat{\ell}$ from the inertial relative navigation filter of Sec. III, the unit vector $\underline{u}^{\mathfrak{F}_I}$ can be calculated now in the inertial frame.

Assuming that the boresight unit vector $\underline{b}^{\mathfrak{F}_b}$ is initially aligned with the x_I axis of the inertial frame, the quaternion command q_{cI} to align $\underline{b}^{\mathfrak{F}_b}$ with $\underline{u}^{\mathfrak{F}_I}$ is given by [28,29]

$$q_{cI} = \frac{1}{\sqrt{2(1+\underline{b}\cdot\underline{u})}} \times \left[(\underline{b}\times\underline{u})\cos\frac{\phi}{2} + (\underline{b}+\underline{u})\sin\frac{\phi}{2};\ (1+\underline{b}\cdot\underline{u})\cos\frac{\phi}{2}\right] \tag{24}$$

where the subscript cI implies *from the inertial frame to the commanded chaser body frame*; the vector part of the quaternion is written first and then the scalar; and ϕ is a roll angle about the boresight or the LOS vector, used to orient the solar arrays of the satellite normal to the sun. The angle ϕ is not relevant in this paper; therefore, for $\phi = 0$, q_{cI} simplifies to

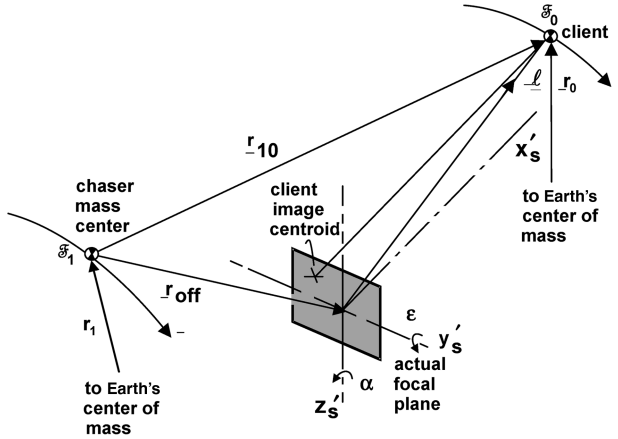

Fig. 7 Relative geometry of the two satellites and the imaging-sensor focal plane.

$$q_{cI} = [\underline{b} \times \underline{u}; 1 + \underline{b} \cdot \underline{u}]/\sqrt{2(1 + \underline{b} \cdot \underline{u})} \tag{25}$$

If the inertial frame in Eq. (25) is replaced with the sensor frame $\mathfrak{F}_s$, the quaternion command q_{cs} then can be related with the small azimuth and elevation angles on the focal plane shown earlier in Fig. 6. The boresight (and laser beam) unit vector $\underline{b}$ in the sensor coordinate frame is $b = [1;\ 0;\ 0]$, and the LOS unit vector $\underline{u}$ in the same frame is $\underline{u} = [x_s/r;\ y_s/r; z_s/r]$, where x_s, y_s, and z_s are the coordinates of the client satellite relative to the chaser satellite in its sensor frame. Applying Eq. (25), the quaternion command to align the sensor boresight axis and the laser beam with the line-of-sight vector $\underline{\ell}$ is found to be

$$q_{cs} = \begin{bmatrix} [0;\ -z_s/r;\ y_s/r] \\ 1 + x_s/r \end{bmatrix} \Big/ \sqrt{2(1 + x_s/r)} \tag{26}$$

Linearizing the definitions of the azimuth and elevation angles in Eq. (20) for small angles, the quaternion command (26) can be approximated as $q_{cs} \approx ([0;\ \varepsilon/2;\ \alpha/2];\ 1)$, where $x_s \approx r$ and $|(y_s, z_s)| \ll x_s$. The focal-plane sensor measures these angles at 1 Hz frequency, as modeled in Eqs. (20). These 1 Hz measurements are processed along with the 50 Hz gyro measurements and every 6 s star tracker measurements by the inertial relative navigation EKF to produce the line-of-sight vector estimate $\hat{\ell}$ and the velocity estimate $\dot{\hat{\ell}}$ at 50 Hz in the inertial frame. These estimates are then used in Eq. (25) to obtain the inertial quaternion commands (and rate commands, derived next) at 10 Hz (Fig. 1) and to generate the focal-plane angle estimates $\hat{\varepsilon}$ and $\hat{\alpha}$ at 25 Hz. These estimates are the y and z components of the 25 Hz attitude error signal $\underline{\theta}_e$ in Fig. 1 for the PID attitude controller. Note that the 1 Hz noisy focal-plane measurements themselves are not enough to point the sensor with the required accuracy at the client satellite.

B. Angular-Rate Commands

To stabilize the imaging sensor on the client satellite, the rate command $\underline{\omega}_{cI}$ is required, which is related to the inertial velocity of the LOS vector $\dot{\ell}$, which, in the chaser body frame $\mathfrak{F}_b$, is

$$\underline{\dot{\ell}}^{\mathfrak{F}_b} = \underline{C}_{bI}(\underline{\dot{r}}_0^{\mathfrak{F}_I} - \underline{\dot{r}}_1^{\mathfrak{F}_I}) - \underline{\omega}_{bI} \times \underline{r}_{\text{off}}^{\mathfrak{F}_b} \tag{27}$$

and $\underline{\omega}_{bI}$ is the inertial angular velocity of the chaser body frame. With the aid of relative navigation, the right side of Eq. (27) is completely known. The inertial angular velocity of the LOS vector in the chaser body frame is then [30]

$$\underline{\omega}_{cI} = \underline{\ell}^{\mathfrak{F}_b} \times \underline{\dot{\ell}}^{\mathfrak{F}_b}/(\underline{\ell} \cdot \underline{\ell}) \tag{28}$$

To illustrate a scalar version of Eq. (28), suppose the sensor boresight is pointed exactly at the client satellite so that, in the sensor frame, $\underline{\ell} = [x_s, 0, 0]^T$. Suppose further that the inertial relative velocity of the target in the sensor frame is $\dot{\ell} = [v_{xs},\ v_{ys},\ v_{zs}]^T$. Equation (28) then yields the inertial rate command for the chaser satellite in the sensor frame as

$$\underline{\omega}_{cI}^{Fs} = [0;\ -v_{zs}/x_s;\ v_{ys}/x_s] \tag{29}$$

Equation (29) indicates that, first, there is no rotational rate command about the sensor's x_s axis, as expected, and, second, if the two satellites get closer without reducing their relative velocity, the rate commands will become larger, as one should expect. On the other hand, a multipulse glideslope guidance, if employed, will exponentially reduce both relative position and relative velocity between the two satellites, resulting in containment of the rate commands. This will be illustrated in Sec. V.

V. Steady-State Three-Axis Attitude Estimation with Gyros and Star Trackers

Although the SIGI provides an estimate of the inertial attitude of the chaser satellite in flight, a new steady-state three-axis attitude estimator is presented here that facilitates the simulation of the present study. Much has been written on the attitude estimation in the last few decades with varying degrees of detail and complexity; see [27] for a recent attitude estimator based on the Bortz equation. In this section, however, we generalize a simple, constant-gain, steady-state single-axis technique of gyro measurement update with star tracker measurements developed in [31] to three-axis.

A. Attitude Measurements Using Gyros and Star Trackers

Following [31], the spacecraft attitude is measured with gyros at an interval of τ (5 ms, presently) at $t = k\tau$ ($k = 1, 2, \ldots, n$) and also with a star tracker at an interval of $T = n\tau$. The index k is reinitialized to 0 when it is equal to n. The three-axis incremental angle $\Delta\underline{\phi}_k$ measured by the gyros during the interval $t_{k-1} \le t \le t_k$ is

$$\Delta\underline{\phi}_k = \Delta\underline{\theta}_k + \tau\underline{b}_k + \underline{\beta}_k + \underline{q}_k \tag{30}$$

where $\Delta\underline{\theta}_k$ is the true change in the spacecraft attitude, $\underline{b}_k$ is the drift rate of the gyro, $\underline{\beta}_k$ is a zero-mean noise in the measurement arising from a 3×1 random-walk rate $\underline{n}_v(t)$ and a 3×1 drift acceleration $\underline{n}_u$ (see [31]). The variance of $\underline{\beta}_k$ is a 3×3 diagonal matrix for which each element is $\sigma_\beta^2 = \sigma_v^2\tau + \sigma_u^2\tau^3/3$, where σ_v^2 (rad^2/s) and σ_u^2 (rad^2/s^3) are power spectral densities of the scalar elements of $\underline{n}_v$ and $\underline{n}_u$. The 3×1 vector $\underline{q}_k$ in Eq. (30) is a quantization noise in the measurement, noncumulative because each successive addition of the angle $\Delta\underline{\phi}_k$ does not cause it to accumulate, unlike the noise $\underline{\beta}_k$. The quantization noise is not white, but it is treated here as a readout noise of power spectral density equal to $\sigma_e^2 = q^2/12$, where q denotes the angle per quantum signal of the gyro. In the sample period $t_{k-1} \le t \le t_k$, the drift rate $\underline{b}_k$ may change, and this change is modeled in vector notations as

$$\underline{b}_k = \underline{b}_{k-1} + \underline{\alpha}_k \qquad \underline{\alpha}_k = N(\underline{0}, \underline{\sigma}_\alpha) \tag{31}$$

where $\underline{\alpha}_k$is a zero-mean discrete random-rate noise vector and the variance of each of its element is [31] $\sigma_\alpha^2 = \sigma_u^2\tau$.

The estimate of the incremental angle $\Delta\underline{\theta}_k$, denoted as $\Delta\hat{\underline{\theta}}_k$, is obtained from the gyro output $\Delta\underline{\phi}_k$ as follows:

$$\Delta\hat{\underline{\theta}}_k = \Delta\underline{\phi}_k - \tau\hat{b}_k \tag{32}$$

$$\hat{b}_k = \hat{b}_{k-1} \tag{33}$$

where $\hat{b}_k$ is the estimate of the drift rate $\underline{b}_k$, estimated with the aid of the star tracker measurements. The inertial attitude of the spacecraft is obtained recursively from $\hat{C}_{kI} = \hat{C}_{k,k-1}\hat{C}_{k-1,I}$, where, in terms of $\Delta\hat{\underline{\theta}}_k$ and its antisymmetric matrix counterpart $\Delta\hat{\underline{\theta}}_k^\times$, the incremental direction cosine matrix is

$$\hat{C}_{k,k-1} = \underline{1} - \Delta\hat{\underline{\theta}}_k^\times + [\Delta\hat{\underline{\theta}}_k\Delta\hat{\underline{\theta}}_k^T - \|\Delta\hat{\underline{\theta}}_k\|^2\underline{1}]/2 \tag{34}$$

and $\underline{1}$ is a 3×3 identity matrix. Also, $\hat{C}_{kI}$ is the estimate of the spacecraft inertial attitude at $t = t_k$ relative to an inertial frame. When $k = n$, a star tracker provides the spacecraft attitude, equal to $\underline{C}_{n\cdot\text{st},I}$ relative to the inertial frame. This involves a 3×1 star tracker angle noise vector $\underline{\nu}_{\text{st}}$; thus,

$$\underline{C}_{n.\text{st},I} = (\underline{1} - \underline{\nu}_{\text{st}}^\times)\underline{C}_{nI} \tag{35}$$

where $\underline{C}_{nI}$ is the true spacecraft attitude at $k = n$ and $t = t_n$. The three elements of the zero-mean random Gaussian noise vector $\underline{\nu}_{\text{st}}$ may be all different, depending on the number of start trackers and their orientations relative to the spacecraft axes. The low- and high-frequency spatial noise in star tracker measurements is ignored here [32,33].

B. Steady-State Gyro Updates Using Star Tracker Measurements

To formulate this update for a three-axis attitude estimator, we first note the steady-state correction of the single-axis gyro-measured

attitude with star tracker measurements at $k = n$, following [31]. Let $\hat{\theta}_n \triangleq \hat{\theta}_0(-)$ be the gyro-estimated spacecraft attitude just before the star tracker measurement, and let θ_{st} be the spacecraft attitude measured by the star tracker at that time. Then the estimate $\hat{\theta}_0(-)$ is updated to $\hat{\theta}_0(+)$; thus,

$$\hat{\theta}_0(+) = \hat{\theta}_0(-) + (1 - \zeta^{-2})[\theta_{\text{st}} - \hat{\theta}_0(-)] \tag{36}$$

where the parameter ζ is defined subsequently. Recall that the subscript n is replaced with 0, and the star tracker update is performed periodically at $k = n$ with the period $T = n\tau$.

A three-axis equivalent of Eq. (36) is developed as follows. Denote the gyro-estimated spacecraft attitude at $k = n$ as $\hat{\underline{C}}_{n\cdot\text{gyro},I}$, where the subscript gyro distinguishes this attitude matrix from the star-tracker-measured attitude matrix $\underline{C}_{n\cdot\text{st},I}$ [Eq. (35)]. Analogous to Eq. (35), $\hat{\underline{C}}_{n\cdot\text{gyro},I}$ has an accumulated estimation error equal to $\underline{\nu}_{n\cdot\text{gyro}}$ and, symbolically,

$$\hat{\underline{C}}_{n.\text{gyro},I} = (\underline{1} - \hat{\nu}^{\times}_{n\cdot\text{gyro}})\underline{C}_{nI} \tag{37}$$

Because the true attitude $\underline{C}_{nI}$ is unknown, the estimation error angle $\hat{\nu}_{n\cdot\text{gyro}}$ is unknown also.

The three-axis equivalent of the small angle $\theta_{\text{st}} - \hat{\theta}_0(-)$ in Eq. (36) is

$$\theta_{\text{st}} - \hat{\theta}_0(-) \Leftrightarrow \underline{C}_{n\cdot\text{st},I}\hat{\underline{C}}_{I,n\cdot\text{gyro}} \tag{38a}$$

$$\approx \underline{1} - (\underline{\nu}_{\text{st}} - \hat{\nu}_{n\cdot\text{gyro}})^{\times} \tag{38b}$$

$$\triangleq \underline{1} - \underline{\nu}^{\times}_{\text{st/gyro}} \tag{38c}$$

Because both $\underline{C}_{n\cdot\text{st},I}$ and $\hat{\underline{C}}_{n\cdot\text{gyro},I}$ are known, the multiplication in Eq. (38a) can be performed and the small angle error vector $\hat{\nu}_{\text{st/gyro}}$, defined by Eqs. (38b) and (38c), can be calculated. The error angle $\hat{\nu}_{\text{st/gyro}}$ is a 3×1 relative error angle vector between the star tracker measurements and the gyro-estimated attitude.

To incorporate the update factor $1 - \zeta^{-2}$ of Eq. (36) in the three-axis attitude estimation technique, we recognize that the parameter ζ, defined subsequently by Eq. (45), depends on the star tracker measurement noise for the axis at hand. Hence, each of the three elements $\nu_{\text{st/gyro},\alpha}$ $(\alpha = x, y, z)$ of $\underline{\nu}_{\text{st/gyro}}$ is corrected to $(1 - \zeta_{\alpha}^{-2})\nu_{\text{st/gyro},\alpha}$. To abbreviate the notations, introduce

$$\underline{\nu}_{\text{st/update}} \triangleq \begin{bmatrix} (1 - \zeta_x^{-2}) & \nu_{\text{st/gyro},x} \\ (1 - \zeta_y^{-2}) & \nu_{\text{st/gyro},y} \\ (1 - \zeta_z^{-2}) & \nu_{\text{st/gyro},z} \end{bmatrix} \tag{39}$$

Then the following three-axis equivalent of Eq. (36) is written by inspection:

$$\hat{\underline{C}}_{0\cdot\text{gyro},I}(+) = [\underline{1} - \underline{\nu}^{\times}_{\text{st/update}}]\hat{\underline{C}}_{n\cdot\text{gyro},I} \tag{40}$$

With regard to the gyro bias, the three-axis update of the bias vector $\hat{b}_n \triangleq \hat{b}_0(-)$ following the single-axis update [31] is

$$\hat{b}_0(+) = \hat{b}_0(-) - \begin{bmatrix} S_{u,x}(\zeta_x T)^{-1}\nu_{\text{st/gyro},x} \\ S_{u,y}(\zeta_y T)^{-1}\nu_{\text{st/gyro},y} \\ S_{u,z}(\zeta_z T)^{-1}\nu_{\text{st/gyro},z} \end{bmatrix} \tag{41}$$

where the dimensionless parameter $S_{u,\alpha}$ for $\alpha = (x, y, z)$ is defined subsequently.

To compare gyro noise with the star tracker noise, [31] introduced the following three dimensionless parameters for each axis of the spacecraft.

Readout noise:

$$S_e = \sigma_e/\sigma_{\text{st}} \tag{42}$$

Random-walk noise:

$$S_v = T^{1/2}\sigma_v/\sigma_{\text{st}} \tag{43}$$

Drift angle:

$$S_u = T^{3/2}\sigma_u/\sigma_{\text{st}} \tag{44}$$

The parameter ζ is defined in terms of the preceding three dimensionless parameters:

$$\zeta = \gamma + \tfrac{1}{4}S_u + \tfrac{1}{2}(2\gamma S_u + S_v^2 + \tfrac{1}{3}S_u^2)^{1/2} \tag{45}$$

where

$$\gamma = (1 + S_e^2 + \tfrac{1}{4}S_v^2 + \tfrac{1}{48}S_u^2)^{1/2} \geq 1 \tag{46}$$

The covariances of the attitude and the bias estimation errors and their correlations are given in [31].

VI. Numerical Results and Discussion

To illustrate the preceding closed-loop inertial relative navigation, attitude pointing and sight-line stabilization, and steady-state Kalman filter for attitude estimation, we consider two spacecraft: an active (chaser) spacecraft at an altitude of 500 km and a client spacecraft 10 km above, ~18 km ahead, and ~8 km across the orbit plane, the inclination angles of both orbits being 46 deg. The difference between the ascending-node angles of the two orbits is 0.1 deg, and the two orbits are circular except for the J_2 gravitational effect. Because the two spacecraft are in almost the same orbit and almost exactly circular, the inertial position and velocity of the client spacecraft would be weakly observable, according to [4]. We perform glideslope guidance of the active spacecraft from its current position to 1 km behind and 1 km below the client spacecraft. The noise sources considered in the simulation are gyros and star tracker measurement noises, imaging-sensor noise, and GPS-based inertial navigation errors of the active spacecraft. The overall guidance, navigation, and control performance of the closed-loop system is illustrated and discussed subsequently.

A. Attitude Estimation Errors Using Three-Axis Gyros and a Star Tracker

Noise statistics of the gyros and the star tracker and the three associated nondimensional parameters S_e, S_u, and S_v are as follows. The gyro noise parameters are bias (drift rate) of 0.02 μrad/s, rate of change of bias σ_u of 4.0e-12 rad/s$^{3/2}$, random-walk rate σ_v of 0.75 μrad/s$^{1/2}$, quantization as white noise σ_e (readout noise and electronic noise) of 1.6 $(5.4/\sqrt{12})$ μrad.

The star tracker noise σ_{st} parameters are focal-plane axis (1σ per axis), 35 μrad, and boresight axis (1σ), 280 μrad.

The dimensionless parameters comparing gyro noise with star tracker noise $\sigma_{\text{st}} = 35$ μrad are (with T or the star tracker measurement interval) readout noise $S_e = \sigma_e/\sigma_{\text{ST}} = 0.05$, drift rate change parameter

$$S_u = T^{3/2}\sigma_u/\sigma_{\text{st}} = \begin{cases} 10^{-7} & \text{for} \quad T = 1 \text{ s} \\ 6\text{e}^{-4} & \text{for} \quad T = 300 \text{ s} \end{cases}$$

and the random walk parameter

$$S_v = T^{1/2}\sigma_v/\sigma_{\text{st}} = \begin{cases} 0.02 & \text{for} \quad T = 1 \text{ s} \\ 0.37 & \text{for} \quad T = 300 \text{ s} \\ 1 & \text{for} \quad T = 2177 \text{ s } (\sim 36 \text{ min}) \end{cases}$$

The corresponding steady-state attitude estimation error versus star tracker measurement interval T is displayed in Fig. 8. The star tracker boresight is on the negative x-axis side, tilted toward the zenith by 15 deg. In the star tracker frame, the star tracker noise is 35 μrad about each focal-plane axis and 280 μrad about its boresight, as stated earlier, but because of the tilt angle, the projection of the star tracker noise about the spacecraft roll, pitch, and yaw axes

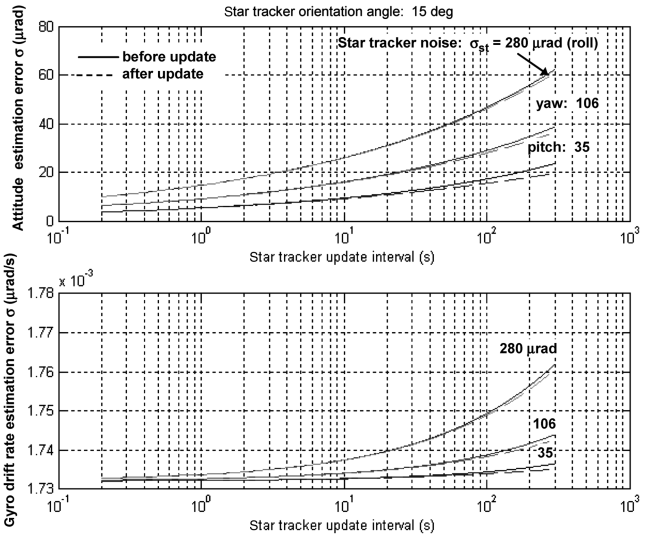

Fig. 8 Roll, pitch, yaw attitude, and drift rate estimation errors before and after star tracker updates versus the update interval.

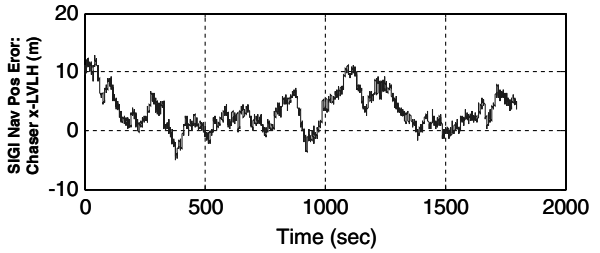

Fig. 9 GPS-based inertial navigation errors of the chaser satellite position error along the *x*-LVLH axis.

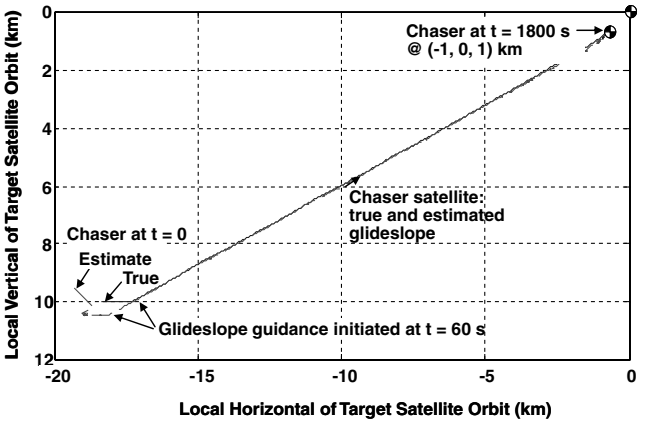

Fig. 10 True and estimated chaser satellite positions relative to the client satellite in the client's LVLH frame.

is 280, 35, and 106 μrad. Because of the random walk of the gyros, the steady-state attitude estimation errors of the gyros/star tracker using the steady-state attitude Kalman filter grow with T. On the lower end of T, toward 0.2 s, the standard deviation of the attitude estimation error $\sigma_{\tilde{\theta}}$ approaches the quantization noise $\sigma_q = 1.6$ μrad of gyros, and the attitude estimation error $\sigma_{\tilde{\theta}}$ before and after the star tracker update are about the same because σ_{st} is much larger, the minimum being 35 μrad about the pitch axis. On the upper end of T, as T increases, $\sigma_{\tilde{\theta}}$ rises toward the star tracker noise σ_{st}, dropping some cyclically with each star tracker measurement update. Regarding the selection of T, [32,33] recommend 6 s for low Earth orbits, so that the low- and the high-frequency spatial noises in the star tracker measurements, not modeled here, become negligible. For more illustration on attitude estimation performance of the filter presented here, see [14].

B. SIGI Navigation Errors of the Chaser Satellite

One record of the exponentially correlated position errors along the instantaneous x-LVLH axis is illustrated in Fig. 9 for 1800 s. The parameters of these errors were stated earlier: standard deviation of the bias, $\sigma_b = 5.1$ m, time constant $= 1/\beta_b = 12.5$ min, standard deviation of the random error $= 1.4$ m, and time constant $= 60$ s. The inertial velocity errors are white noise with 0.03 m/s (1σ). These errors typify 50th-percentile accuracies of GPS inertial navigation with a precision-positioning service [22]. The corresponding 3×3 $\underline{Q}_{\text{pos}}$ and $\underline{Q}_{\text{vel}}$ process noise matrices are used with zero cross-correlation while propagating the 6×6 error covariance matrix $\underline{P}$.

C. Imaging Sensor Noise

As distance r of the imaging sensor from the client satellite decreases, the image size on the focal plane increases [9] and, correspondingly, standard deviation of the measurement noise increases. Specifically, the noise statistics for each axis of the focal plane are 70 μrad for $7 \leq r \leq 10$ km, 175 μrad for $3 \leq r \leq 7$ km, and 350 μrad for $1 \leq r \leq 3$ km. It is instructive to compare these with the attitude estimation error $\sigma_{\tilde{\theta}}$ of the gyros and star tracker in Fig. 8 for star tracker measurement updates at a 6 s interval: $\sigma_{\tilde{\theta}} = \sim 8$ μrad for the y and z axes (pitch and yaw axes) of the spacecraft with a star tracker boresight along the x axis, antiparallel to the imaging-sensor boresight. Clearly, 8 μrad attitude estimation error is negligible compared with the lowest imaging-sensor noise of 70 μrad at long distances. For this reason, the gyros and star tracker noises are not included in the simulation results. Furthermore, to compare zero-mean imaging-sensor noise with the SIGI errors, the angle noise converted to length is 0.7 m at 10 km, 1.225 m at 7 km, and 1.05 m at 3 km. Apparently, these errors are about one-tenth of the GPS inertial navigation errors in Fig. 9, but note that the GPS/INS errors are biased by ~ 6 m and have a zero-mean random error of 1 m standard deviation, about the same as that of the imaging sensor. Note also that the imaging-sensor noise pertains to the measurements (the $\underline{R}$ matrix), whereas the GPS/INS errors pertain to the process noise (the $\underline{Q}$ matrix).

D. Inertial Relative Navigation and Glideslope Guidance

In the presence of the GPS/INS errors and the imaging-sensor noise just illustrated, Fig. 10 portrays a true glideslope trajectory of the chaser satellite approaching the client satellite and the trajectory estimate starting from the initial position (-18, -8, and 10 km) to the final position (-1, 0, and 1 km) in the client satellite's LVLH frame. In the simulation, the spherical plus J_2 gravitational acceleration is modeled, and therefore the osculating LVLH frame is calculated at 10 Hz frequency. The LVLH frame is not used for navigation, guidance, or control purposes; it is used only as a visual aid. The initial relative position and velocity estimation errors of the client satellite are 1, 0.5, and 0.5 km and 0.5, 0.5, and 0.5 m/s, and the initial error covariance matrix $\underline{P}$ $(t = 0)$ is specified accordingly. The measurement matrix $\underline{R}$ and the process noise matrix $\underline{Q}$ are specified as explained earlier. The guidance pulses are at an interval of 60 s starting from $t = 60$ s. Note that the initial position estimation error (1, 0.5, and 0.5 km) is much greater than the SIGI navigation errors (Fig. 9) or imaging-sensor noise expressed in length (0.7 m at 10 km). For this reason, the relative position estimation error and the error covariance matrix $\underline{P}$ decrease substantially with the first few 1 Hz measurements of the imaging sensor, as can be inferred from Figs. 10 and 11 near $t = 0$. The next major reduction in the estimation errors and the error covariances occur with the first guidance pulse at $t = 60$ s, as we observe in Fig. 11a. Subsequently, although y-relative estimation error decreases steadily and becomes bounded by the corresponding $\pm\sqrt{P_{yy}}$, the x and z errors and their velocity counterparts in Fig. 11b struggle to do so. There are several possible reasons: weak observability as stated earlier, biases in SIGI

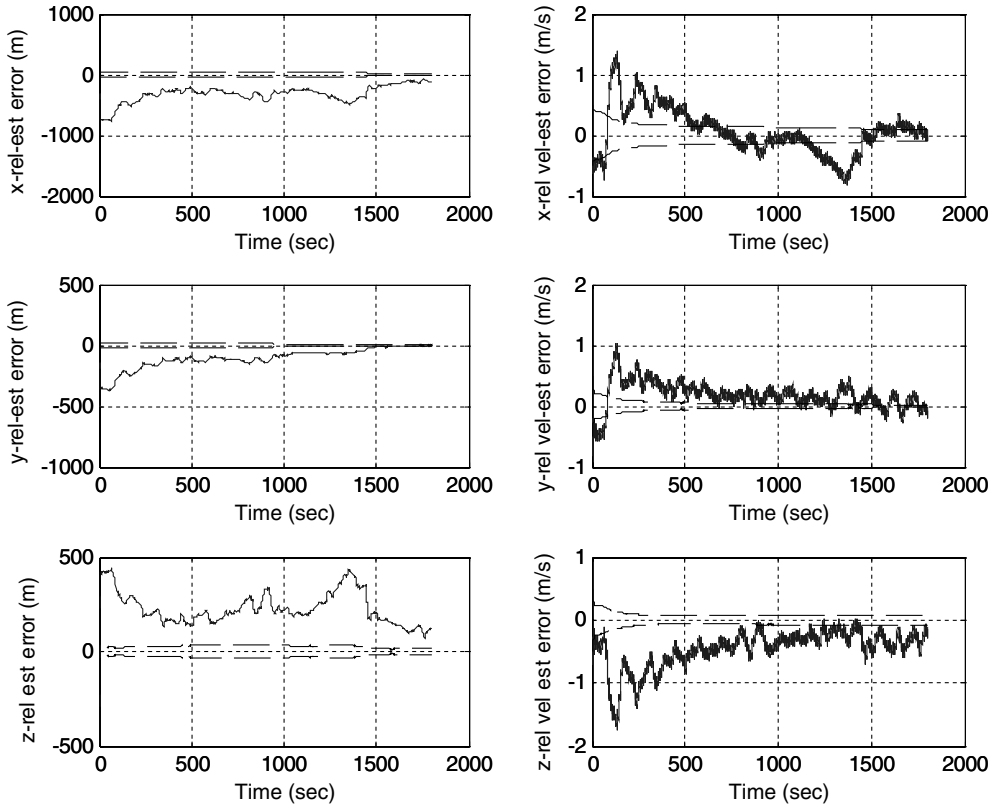

a) Relative position estimation error **b) Relative velocity estimation error**

Fig. 11 Estimation errors in the client's LVLH frame, compared with corresponding ± standard deviation.

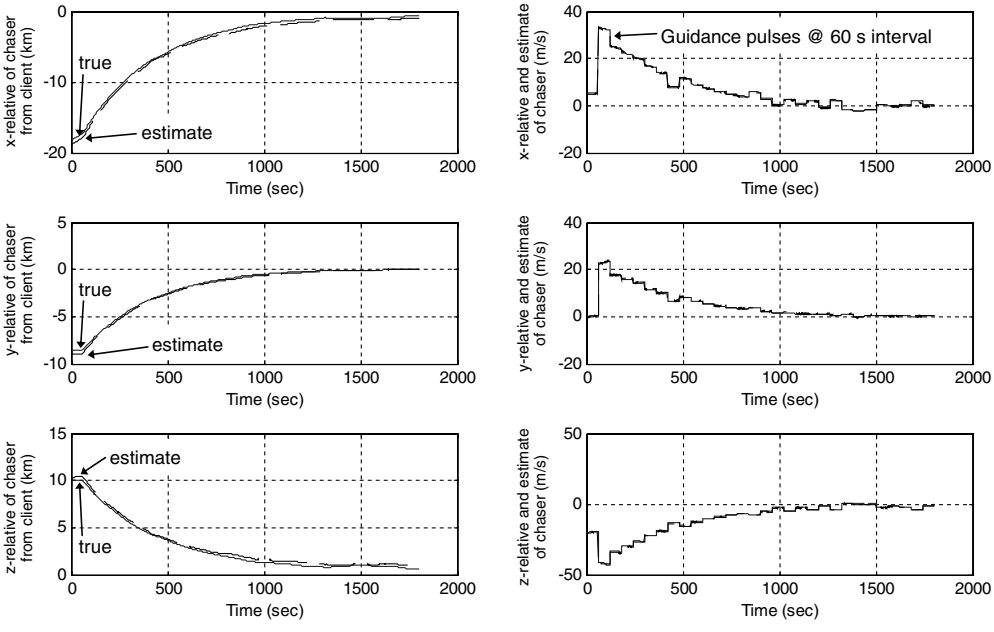

a) Relative position **b) Relative velocity**

Fig. 12 True and estimated relative position and relative velocity of the chaser in the client satellite's LVLH frame; glideslope guidance is active.

navigation errors, lack of range measurements, a constantly precessing local LVLH frame due to the J_2 effect, and the selected $\underline{Q}$ matrix with $q_{\text{scalar}} = 0.001$ not being tuned enough.

The components of the true and the estimated relative positions and velocities of the chaser from the client spacecraft are shown in Figs. 12a and 12b. The exponential decrease of the relative position to -1, 0, and 1 km in 1800 s is apparent. The relative velocity components step up initially with the first guidance pulse at $t = 60$ s to suitable values to follow the stipulated glideslope guidance, and then they are brought discretely and exponentially to the low values specified at 1800 s with 29 periodic firings at each 60 s interval. These components of the $\Delta\underline{v}$ pulses every 60 s in the LVLH frame are shown in Fig. 13, in which we observe that the first pulse is the largest and the subsequent pulses are much smaller.

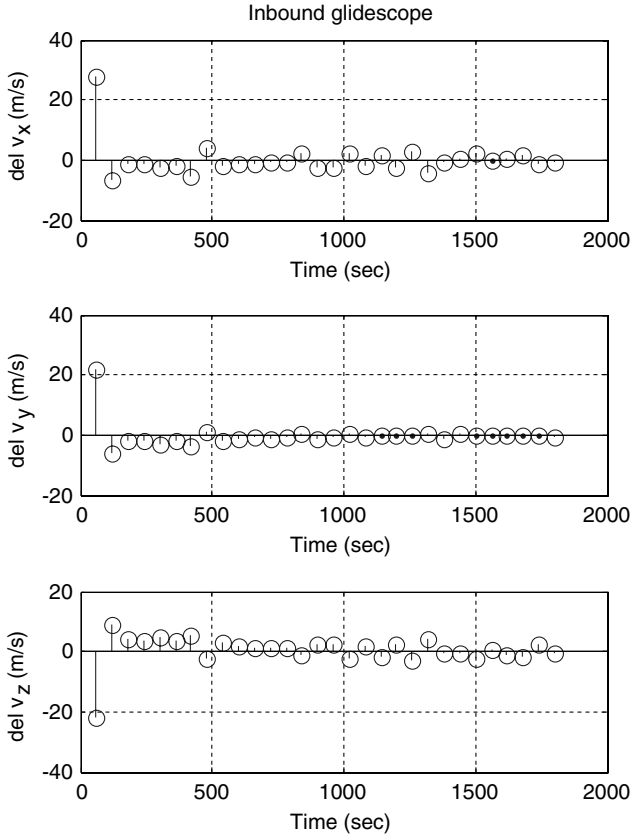

Fig. 13 Glideslope guidance pulses in the client's LVLH frame at 60 s intervals for rendezvous.

E. Attitude Control and Stabilization of the Integrated Sensor's Sight Line

The inertial relative navigation and guidance performance just discussed is realized with a PID attitude controller of bandwidth 0.064 Hz, equal to 360 times the orbital frequency, and sampling frequency of 25 Hz (see Fig. 1). Reaction wheels are used as actuators. Hablani [14] presents a detailed pointing-accuracy analysis and performance of the controller. Here, to conserve space, we limit the portrayal of performance to the focal-plane image coordinates expressed as angles of rotation about the focal-plane y and z axes. It is explained in Sec. IV that in the absence of all measurement noises and navigation errors, the focal-plane image angles are, in fact, equal to the attitude control error signals about the y and z axes: that is, θ_{ey} and θ_{ez} components of $\underline{\theta}_e$ in Fig. 1. In reality, the attitude error signals and the actual focal-plane image angles differ in some respects. Attitude error signal vector $\underline{\theta}_e$ depends on the attitude command estimates and the attitude estimates, which are both affected by the navigation errors and the gyro/star tracker noises, attenuated by the navigation Kalman filter and the attitude Kalman filter. The image on the focal plane, in contrast, exhibits a low-frequency motion because the focal plane (that is, its carrier, the spacecraft bus) is controlled by a low-bandwidth (0.064 Hz, corresponding to a period of 15.6 s) attitude controller. This difference is seen in Fig. 14a, which depicts the two quantities for the y axis with just the sensor noise. Whereas the image angle on the focal plane about the y axis exhibits low-frequency, slightly growing, oscillation, the attitude error signal at 25 Hz has high-frequency contents with amplitudes less than the amplitudes of the image angle. Figure 14b, on the other hand, shows the image angle and the attitude error about the y axis under SIGI navigation errors. We observe that the image angle (that is, the pointing error) is considerably larger than the focal-plane-noise standard deviation per axis (70–350 μrad for the 10–1 km relative range), which steps up as the range decreases. Comparing the pointing accuracy in Fig. 14b with the pointing accuracy in the absence of the SIGI navigation errors in Fig. 14a, we conclude that the image motion is mostly caused by the zero-mean

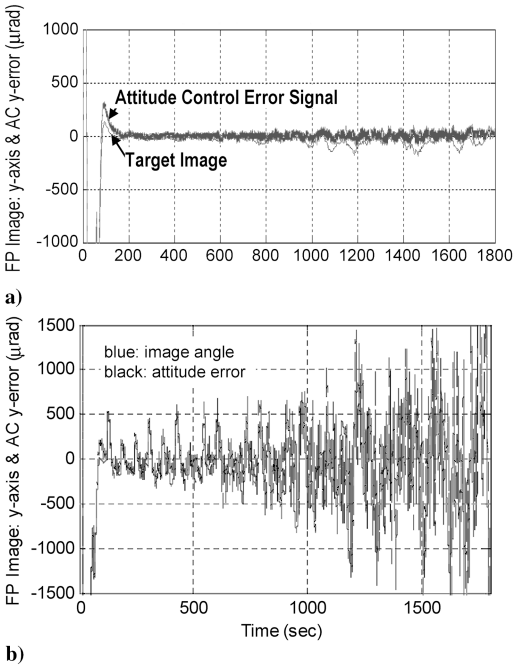

Fig. 14 Elevation angle of the image on the focal plane (FP) and attitude control (AC) y error.

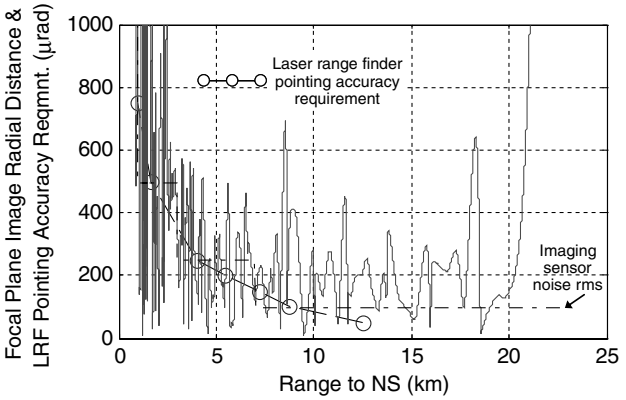

Fig. 15 Target image RSS angle on the focal plane compared with imaging-sensor measurement noise and laser range-finder pointing requirement (NS is the client satellite).

SIGI noise, with rms = 0.5–1.0 m causing a 100 μrad rms image motion at 10 km and a 1000 μrad rms at 1 km, agreeing with the results seen in Fig. 14b. The bias position errors in the SIGI navigation errors of the chaser (Fig. 9), similar to the gyro and star tracker misalignments in [14], do not offset the image from the focal-plane center.

Finally, Fig. 15 shows the root of the sum of squares (RSS) of the y and z image angles and compares it with the RSS of the imaging-sensor noise and the pointing-accuracy requirement for the laser range finder to measure the relative range of the client satellite. For the range less than 12 km, the pointing-accuracy requirement of the laser range finder is met only occasionally and, when met, a relative range measurement arises. In the current simulation, this range measurement is not used in the EKF, however; otherwise, the focal-plane pointing accuracy would improve further and enable progressively more frequent range measurements.

VII. Conclusions

In this paper, a new sight-line-stabilized inertial relative navigation system is presented for midrange (20–1 km) rendezvous of an active chaser satellite with a passive client satellite. The chaser satellite is stabilized to track the client satellite with an integrated

sensor ensemble consisting of an imaging sensor, a coboresighted laser range finder, the space-integrated GPS/INS (SIGI), and a star tracker. A new six-state continuous-discrete extended Kalman filter is developed for inertial relative navigation of the client satellite. A steady-state three-axis inertial attitude estimator is developed for the chaser satellite. The numerical results illustrate that this ensemble carries out a successful midrange rendezvous solely with the azimuth- and elevation-angle measurements locating the client satellite without range measurements. The relative position estimation errors are not necessarily within their standard deviation bounds, and in this respect, the relative navigation filter requires further improvement. But this and Monte Carlo runs must be deferred to future studies. Nonetheless, the attitude controller maintains the client satellite within the imaging-sensor track box amidst the SIGI navigation errors and the client satellite's location estimation errors in the inertial frame. The pointing accuracy achieved with the imaging sensor enables the coboresighted laser range finder, which requires stringent pointing accuracy, to occasionally measure the instantaneous range of the client satellite from the chaser satellite. If used by the relative navigation Kalman filter, these range measurements would improve the pointing accuracy further and effect more frequent range measurements, resulting in more accurate inertial relative navigation of the client satellite and guidance of the chaser satellite.

Acknowledgments

The work reported here was developed under the Autonomous Vehicle Operations Research and Development program and the Orbital Express program. Manny R. Leinz, Anaheim, and Richard Thiel, Huntington Beach, were the Chief Engineers of the two programs, respectively. The author is grateful for the opportunity to be a member of their teams and for approval to publish this work.

References

[1] Bryan, T. C., "Automated Capture of Spacecraft," AIAA Space Programs and Technologies Conference, Huntsville, AL, AIAA Paper 93-4757, Sept. 1993.

[2] Titterton, D. H., and Weston, J. L., *Strapdown Inertial Navigation Technology*, Progress in Astronautics and Aeronautics, Vol. 207, AIAA, Reston, VA, 2004, pp. 475–479.

[3] Moir, I., and Seabridge, A., *Military Avionics Systems*, Wiley, New York, 2006, Sec. 5.7.

[4] Yim, J. R., Crassidis, J. L., and Junkins, J. L., "Autonomous Orbit Navigation of Two Spacecraft System Using Relative Line-of-Sight Vector Measurements," American Astronautical Society, Paper 04-257, 2004.

[5] Hablani, H. B., "Autonomous Relative Navigation, Attitude Determination, Pointing and Tracking for Spacecraft Rendezvous," Guidance, Navigation, and Control Conference, AIAA Paper 2003-5355, Aug. 2003.

[6] Kawano, I., Mokuno, M., Kassai, T., and Suzuki, T., "Results and Evaluation of Autonomous Rendezvous Docking Experiments of ETS-VII," AIAA Guidance, Navigation, and Control Conference, Portland, Oregon, AIAA Paper 99-36780, Aug. 1999.

[7] Park, Y. W., Brazzell, J. P., Jr., Carpenter, J. S., Hinkel, H. D., and Newman, J. H., "Flight Test Results from Real-Time Relative Global Positioning System Flight Experiment on STS-69," NASA TM 104824, Nov. 1996.

[8] Clark, F. D., Spahar, P. T., Brazzell, J. P., Jr., and Hinkel, H. D., "Laser-Based Relative Navigation and Guidance for Space Shuttle Proximity Operations," 26th Annual AAS Guidance and Control Conference, Breckinridge, CO, American Astronautical Society Paper 03-014, Feb. 2003, pp. 1–20.

[9] Gaylor, D. E., and Lightsey, E. G., "GPS/INS Kalman Filter Design for Spacecraft Operating in the Proximity of the International Space Station," AIAA Guidance, Navigation, and Control Conference, Austin, TX, AIAA 2003-5445, Aug. 2003.

[10] Woffinden, D. C., and Geller, D. K., "Relative Angles-Only Navigation and Pose Estimation for Autonomous Orbital Rendezvous," *Journal of Guidance, Control, and Dynamics*, Vol. 30, No. 5, 2007, pp. 1455–1469.
doi:10.2514/1.28216

[11] Bauer, F. H., Hartman, K., and Lightsey, E. G., *Spaceborne GPS: Current Status and Future Visions*, AIAA, Reston, VA, 1998.

[12] Zubkow, Z., "Honeywell SIGI (Space Integrated GPS/INS) H-764G System," American Astronautical Society Paper 03-037, 2003.

[13] Willms, R., "*Space Integrated GPS/INS (SIGI) Navigation System for Space Shuttle*," Inst. of Electrical and Electronics Engineers, Piscataway, NJ, 1999.

[14] Hablani, H. B., "Imaging Sensor Pointing and Tracking Controller Insensitive to Gyros and Star Trackers Misalignments," *Journal of Guidance, Control, and Dynamics*, Vol. 31, No. 4, 2008, pp. 980–990.

[15] Baiocco, P., and Sevaston, G., "On the Attitude Control of a High Precision Space Interferometer," *Space Guidance, Control, and Tracking*, Vol. 1979, Society of Photo-Optical Instrumentation Engineers, Bellingham, WA, 1993, pp. 92–107.

[16] Hablani, H. B., Tapper, M. L., and Dana-Bashian, D. J., "Guidance and Relative Navigation for Autonomous Rendezvous in a Circular Orbit," *Journal of Guidance, Control, and Dynamics*, Vol. 25, No. 3, 2002, pp. 553–562.

[17] Bar-Shalom, Y., Rong Li, X., and Kirubarajan, T., *Estimation with Applications to Tracking and Navigation*, Wiley, New York, 2001, Sec. 3.7.

[18] Fogel, E., and Gavish, M., "*N*-th Dynamics Target Observability from Angle Measurements," *IEEE Transactions on Aerospace and Electronic Systems*, Vol. 24, No. 3, May 1988, pp. 305–308.
doi:10.1109/7.192098

[19] Van der Ha, J., and Mugellesi, R., "Analytic Models for Relative Motion Under Constant Thrust," *Journal of Guidance, Control, and Dynamics*, Vol. 13, No. 4, 1990, pp. 644–650.
doi:10.2514/3.25382

[20] Gelb, A., *Applied Optimal Estimation*, MIT Press, Cambridge, MA, 1974.

[21] Markley, F. L., "Approximate Cartesian State Transition Matrix," *Journal of the Astronautical Sciences*, Vol. 34, No. 2, Apr.–June 1986, pp. 161–169.

[22] Montenbruck, O., and Gill, E., *Satellite Orbits: Models, Methods, and Applications*, Springer, New York, 2000, pp. 205, 293–302.

[23] Misra, P., and Enge, P., *Global Positioning System: Signals, Measurements, and Performance*, 2nd ed., Ganga-Jamuna Press, Lincoln, MA, 2006.

[24] Rogers, R. M., *Applied Mathematics in Integrated Navigation Systems*, AIAA Education Series, AIAA, Reston, VA, 2003, pp. 190–206.

[25] Grewal, M. S., Weill, L. R., and Andrews, A. P., *Global Positioning Systems, Inertial Navigation, and Integration*, Wiley, New York, 2001.

[26] Katzman, M. (ed.), *Laser Satellite Communications*, Prentice–Hall, Upper Saddle River, NJ, 1987, Chap. 6.

[27] Pittelkau, M. E., "Rotation Vector in Attitude Estimation," *Journal of Guidance, Control, and Dynamics*, Vol. 26, No. 6, 2003, pp. 855–860.

[28] Reynolds, R. G., "Quaternion Parameterization and a Simple Algorithm for Global Attitude Estimation," *Journal of Guidance, Control, and Dynamics*, Vol. 21, No. 4, 1998, pp. 669–671.

[29] Markley, F. L., "Fast Quaternion Attitude Estimation from Two Vector Measurements," *Journal of Guidance, Control, and Dynamics*, Vol. 25, No. 2, 2002, pp. 411–414.

[30] Shneydor, N. A., *Missile Guidance and Pursuit Kinematics, Dynamics and Control*, Horwood Publishing, Chichester, England, U.K., 1998, pp. 217–218.

[31] Markely, F. L., and Reynolds, R. G., "Analytic Steady-State Accuracy of a Spacecraft Attitude Estimator," *Journal of Guidance, Control, and Dynamics*, Vol. 23, No. 6, 2000, pp. 1065–1067.

[32] Halsy, D. R., Strikewerda, T. E., Fisher, H. C., and Heyler, G. A., "Attainable Pointing Accuracy with Star Trackers," American Astronautical Society Paper 98-072, 1998.

[33] Wu, Y. W., Li, R., and Robertson, A. D., "Precision Attitude Determination for GOES N Satellites," American Astronautical Society Paper 03-002, 2003.